Delft University of Technology

Lensless single-shot dual-wavelength digital holography with sub-pixel resolution and centimeter depth range

Shangguan, Huangcheng; Urbach, H. Paul; Kalkman, Jeroen

Important note
To cite this publication, please use the final published version (if applicable).
Please check the document version above.

Huangcheng Shangguan ⓘ ; H. Paul Urbach; Jeroen Kalkman ✉ ⓘ

Check for updates

View Online   Export Citation

Articles You May Be Interested In

Artifacts-free lensless on-chip tomography empowered by three-dimensional deconvolution

Appl. Phys. Lett. (August 2024)

Aperture-encoded snapshot hyperspectral imaging with a lensless camera
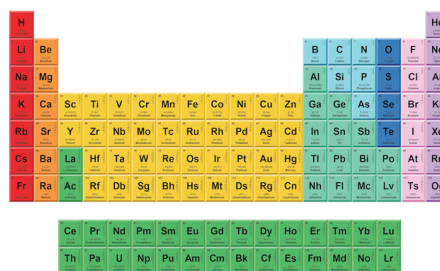
APL Photonics (June 2023)

Lensless polarization camera for single-shot full-Stokes imaging

APL Photonics (November 2022)

AIP Publishing

Lensless single-shot dual-wavelength digital holography with sub-pixel resolution and centimeter depth range

View Online   Export Citation   CrossMark

Huangcheng Shangguan, [ID] H. Paul Urbach, and Jeroen Kalkman[a] [ID]

AFFILIATIONS

Department of Imaging Physics, Delft University of Technology, Lorentzweg 1, 2628 CJ Delft, The Netherlands

[a]Author to whom correspondence should be addressed: j.kalkman@tudelft.nl

ABSTRACT

Lensless single-shot dual-wavelength digital holography is resolution limited by the pixel-size of the camera and often has an insufficient depth range. We present a novel dual-wavelength holographic configuration with expanding wavefront illumination that breaks the pixel-limited resolution barrier and achieves diffraction-limited spatial resolution. By implementing expanding wavefront illumination with dual-wavelength digital holography based on a wavelength-tunable laser, we achieve a high-resolution centimeter-scale depth range. A quantitative precision analysis demonstrates that single-shot acquisition reaches the shot-noise-limited depth detection. The proposed holographic scheme provides a robust 3D optical inspection solution for high-throughput, micro-scale resolution industrial inline metrology.

I. INTRODUCTION

In modern semiconductor manufacturing, device inspection, sample metrology, and defect detection play a critical role in ensuring good product quality and reliability.[1,2] With growing manufacturing complexity, increasing throughput, and reduced sample dimensions, conventional 2D optical inspection methods struggle to meet the demands.[3,4] In high-speed semiconductor production lines, device inspection must not only achieve sub-micrometer 3D surface measurement accuracy but also enable fast, non-contact imaging. Although existing optical 3D imaging techniques—including computational quantitative phase imaging,[5] fringe projection profilometry,[6] and optical coherence tomography[7]—each offer unique advantages, their application in industry is restricted by their limited resolution or need for scanning. Moreover, industrial environments can have vibrations, temperature fluctuations, and air disturbances that further complicate their use. Therefore, developing a 3D imaging technology that balances high resolution, large depth range, and resilience to environmental factors has become an urgent need in industrial inspection.

Off-axis digital holography (DH)[8–10] is an ideal choice for high-speed industrial inspection due to its single-shot, non-contact,

full-field imaging capability and strong robustness against environmental noise.[11–13] However, conventional single-wavelength DH faces the fundamental 2π phase ambiguity limitation.[14–16] This issue occurs when the surface height variations exceed half the illumination wavelength (typically a few hundred nm), leading to 2π phase jumps that compromise the measurement accuracy. This is particularly problematic in industrial products with complex surface topography, as they often feature abrupt height changes that phase unwrapping failures.

Dual-wavelength digital holography (DWDH)[17–19] addresses this issue by combining two interferograms obtained at two different wavelengths. The holograms at the two wavelengths are typically multiplexed onto a single camera, allowing for single-shot DWDH acquisition. By combining the fields of the two wavelengths, a beat wave can be created with a synthetic wavelength that can span hundreds or even thousands of times the wavelength of the individual light sources. DWDH significantly expands the depth range while maintaining the native lateral resolution of the single-wavelength DH systems, making it suitable for measuring complex surfaces with large height variations.[20,21] However, DWDH still faces several challenges in industrial application settings. First, achieving a large depth range requires precise wavelength

selection and stability. For example, to reach centimeter-scale depth ranges, the wavelength difference should be on the order of a few picometers, imposing stringent demands on wavelength accuracy and long-term stability.[22,23] Second, lensless DWDH configurations suffer, despite their advantages in setup compactness and flexibility, from lateral resolution limitations dictated by the detector pixel size.[24,25]

Instead of achieving superresolution through the acquisition of multiple measurements,[26–28] this paper demonstrates improved lateral resolution lensless DWDH using expanding wavefront illumination.[29–32] The proposed method overcomes the lateral resolution limit imposed by the detector finite-pixel size, achieving an enhanced, numerical aperture-limited resolution. With DWDH implemented using a fixed wavelength and a tunable laser, centimeter-scale depth range and numerical-aperture limited resolution were demonstrated. We demonstrate a practical wavelength calibration scheme to ensure accurate height measurement and develop a corresponding phase-retrieval algorithm that corrects for additional expanding wavefront aberrations. Experimental results verify the feasibility of our method, with phase measurement precision approaching the shot-noise limit. The findings and methods presented in this paper are expected to advance the practical application of digital holography in industrial metrology and inspection.

II. METHODS

A. Expanding wave illumination dual-wavelength digital holography setup

The setup for a reflective lensless dual-wavelength digital holography (DWDH) with expanding wavefront illumination (EWI) is illustrated in Fig. 1(a). A He–Ne laser (HRS015B, Thorlabs) with wavelength $\lambda_1 = 632.992$ nm and a tunable laser diode (VBG-0633-020-BFY, Sacher Lasertechnik) with typical central wavelength $\lambda_2 = 633$ nm are used as light sources. Both beams first pass through a beam expander to increase the beam size to cover the entire sample. The beam expander for λ_1 is composed of two positive lenses (LA1805-A and LA1509-A, Thorlabs) and a pinhole (P30K, Thorlabs) and for λ_2 is composed of two lenses (LA1131-A and LA1509-A, Thorlabs) and a pinhole (P25K, Thorlabs). The expanded and collimated beam for λ_1 and λ_2 enter their respective Mach–Zehnder interferometers. For both wavelengths, the light is first split by a cube beam splitter (BS013, Thorlabs) into two beams: a reference beam (R) and an object beam (O). In the reference arm, lens $L2$ (LA1422-A, Thorlabs) is used to focus the reference beam and make an expanding wavefront, which is then reflected by a pellicle beam splitter P2 (BP250, Thorlabs). In the object arm, the beam is reflected by mirror M2, passes through a pellicle beam splitter P1 (BP250, Thorlabs), and is focused by lens $L1$ (LA1422-A, Thorlabs). The sample is illuminated by the expanding wavefronts, and the back-reflected field from the sample is redirected by a beam splitter BS2 (BS013, Thorlabs) to the camera. The object and reference beam interfere in the plane of the camera (MC124MG-SY-UB, XIMEA). The camera has $N_x = 4112$ and $N_y = 3008$ pixels with a uniform pixel pitch of $\Delta x = \Delta y = 3.45$ μm. The case for λ_2 is similar.

Since the two lasers are mutually incoherent, the recorded hologram is the sum of the individual holograms and is recorded simultaneously on the camera. To enable single-shot measurement,[33,34] we
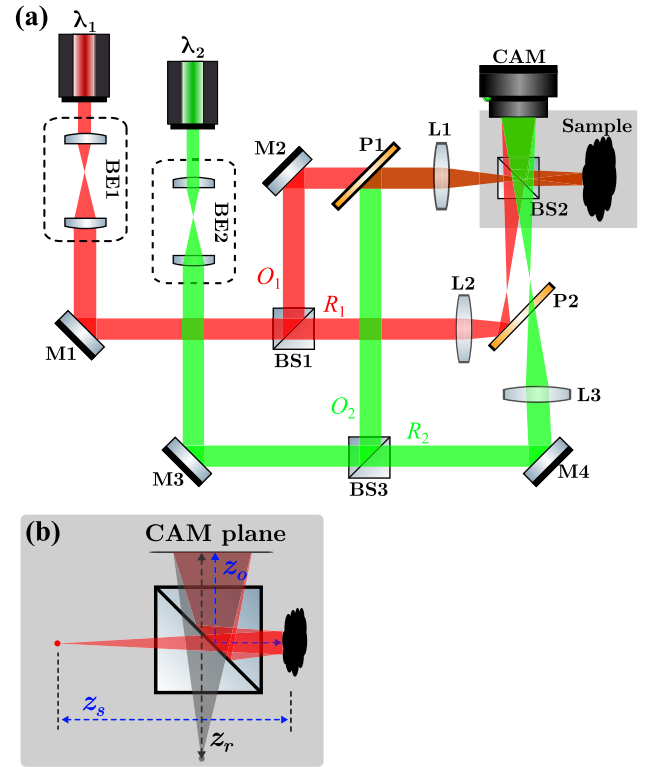

FIG. 1. (a) Schematic diagram of a reflective lensless expanding wavefront DWDH setup (both lasers emit red beam, and the color difference is solely for visual distinction). M, Mirror; BS, beam splitter; L, lens; P, pellicle; and CAM, camera. (b) Zoom-in illustration of the illumination and reference beam. z_o, Sample-to-camera distance; z_s, illumination focal point-to-sample distance; and z_r, reference beam focal point-to-camera distance.

deliberately arrange the two holograms to have distinct interference fringe orientations and employ spatial frequency multiplexing in the Fourier domain. The intensity of the resulting dual-wavelength hologram I_{DW} captured by the camera can be expressed as

$$I_{DW} = \sum_i |O_i|^2 + |R_i|^2 + O_i R_i^* + O_i^* R_i, \quad (1)$$

where O_i and R_i refer to the object and reference fields at the detector plane, respectively, $i = 1, 2$ indicates the two wavelengths, and * is complex conjugation. Assuming the object field at the sample plane is $U(\xi, \eta) = |U| \exp(i\phi_o)$, where ϕ_o is the phase delay introduced by the object. The field O_i, resulting from the object being illuminated by the expanding wavefront and propagating to the camera, can be expressed as

$$O_i(x, y) = \exp\left\{\frac{i\pi}{\lambda_i c_o}(x^2 + y^2)\right\} \cdot \text{Fresnel}_{\frac{z_o}{M_a}}[U(\xi, \eta)]\left(\frac{x}{M_a}, \frac{y}{M_a}\right), \quad (2)$$

where $M_a = (z_o + z_s)/z_s$, z_o is the sample-to-camera distance, and z_s is the distance from the focal point of L1 to the sample, as illustrated in Fig. 1(b). A physical interpretation of (2) is that the object field

$U(\xi, \eta)$ undergoes the Fresnel propagation over a distance z_o/M_a while being magnified by a factor M_a and has a parabolic phase term with curvature c_o. A detailed derivation and exact expression for the curvature c_o is provided in Appendix A. For the off-axis EWI holography configuration, the reference beam is modeled with a paraxial approximation of a spherical wavefront expressed as

$$R_i = |R_i|\exp\left\{\frac{i\pi}{\lambda_i c_r}\left[(x - x_0)^2 + (y - y_0)^2\right]\right\}. \qquad (3)$$

Here, the wavefront curvature parameter c_r corresponds to the distance z_r, which is the distance from the source location of the expanding wave to the camera as defined in Fig. 1(b), while x_0, y_0 are the lateral coordinates of the source location of the reference beam.

In standard off-axis digital holography processing, the off-axis term $O_i R_i^*$ is extracted by Fourier filtering, followed by a back-propagation to retrieve the sample phase ϕ_o. In DWDH, two phase maps ϕ_{o1} and ϕ_{o2} can be retrieved from the dual-wavelength hologram I_{DW}. The synthetic phase or beat phase Φ is calculated with $\Phi = \phi_{o1} - \phi_{o2}$. Assuming a single reflecting surface, the height h can be calculated according to

$$h = \frac{\Phi}{4\pi}\frac{\lambda_1 \lambda_2}{|\lambda_1 - \lambda_2|} = \frac{\Phi}{4\pi}\Lambda, \qquad (4)$$

where $\Lambda = \frac{\lambda_1 \lambda_2}{|\lambda_1 - \lambda_2|}$ is the synthetic wavelength.

B. PWI and EWI DWDH resolution

In conventional lensless digital holography with plane wavefront illumination (PWI), the lateral resolution depends on the numerical aperture (NA) and the size of the pixel. The NA is defined as $NA = \sin(\tan^{-1}[W_{cam}/(2z_o)])$, where W_{cam} is the width of the camera sensor and z_o is the sample-to-camera distance. The resolution for PWI is then $r = 0.82\lambda/NA$, where the factor 0.82 is the proportionality factor commonly used for coherent imaging.[35] However, since the diffracted field is discretely sampled by the sensor, the pixel size Δx limits the lateral resolution. The maximum frequency support of the camera is given by the Nyquist limit, which restricts the lateral resolution to twice the pixel size $2\Delta x$. The achievable resolution is given by the larger one of the two. The resolution of DH is shown in Fig. 2(a), where the dashed line shows the resolution for the PWI-DH system with respect to the sample-to-camera distance z_o for a camera with the specifications as used in our experiment. As the distance decreases, the NA increases, and the diffraction-limited resolution decreases. However, at a certain distance, the diffraction-limited resolution equals twice the pixel size. Thereafter, no matter how much distance is reduced, the resolution no longer improves.

For the case of expanding wavefront illumination (EWI), as shown in the configuration of Fig. 1(b), the optical field from the sample is progressively magnified as it propagates to the camera. The magnification of the field on the camera is $M_a = (z_o + z_s)/z_s$ (see Appendix A for a more detailed derivation). Equivalently, this can be viewed as the effective pixel size being reduced by a factor of M_a in the object plane. We can therefore conclude that, for the pixel size not to limit the spatial resolution, it must hold that

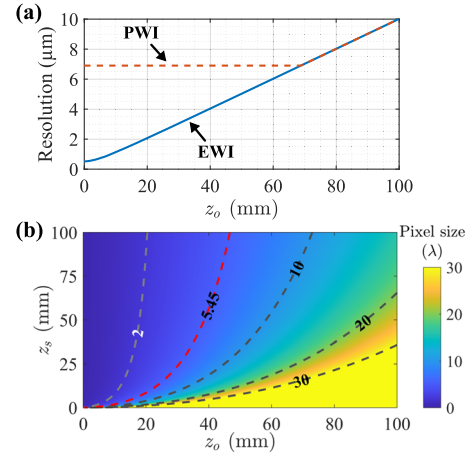$$\frac{2\Delta x}{M_a} \leq 0.82\frac{\lambda}{NA}. \qquad (5)$$

FIG. 2. (a) Comparison of the lateral resolution in plane (PWI) and expanding wavefront illumination (EWI) digital holography. (b) Contour plot of the right-hand side of (6), which indicates the maximum allowed pixel size (in units of wavelength λ) to achieve diffraction-limited resolution.

Substituting $M_a = (z_o + z_s)/z_s$ into the equation and rearranging, we get

$$\frac{\Delta x}{\lambda} \leq \frac{0.41}{\sin\left[\tan^{-1}\left(\frac{W_{cam}}{2z_o}\right)\right]}\frac{z_o + z_s}{z_s}. \qquad (6)$$

Equation (6) indicates that the diffraction-limited resolution is always achievable in the EWI-DH, provided that the system configuration fulfills the required condition. Figure 2(b) shows the contour plot of the right-hand side of (6), representing the maximum allowed pixel size (in units of wavelength λ) for a given setup with specific z_o and z_s to achieve diffraction-limited resolution. The red contour line in Fig. 2(b) shows the pixel size of $\Delta x = 5.45\lambda$ of our setup. The resolution of EWI is depicted by the solid blue line in Fig. 2(a) and shows a close to linear relation between the object distance and resolution.

C. Quantitative phase reconstruction in EWI-DWDH

Extracting the sample phase ϕ_{oi} from the off-axis term $O_i R_i^*$ in EWI-DWDH is more complicated than in conventional PWI-DWDH. The entire data processing for EWI-DWDH is shown in Fig. 3. Since the two wavefront curvatures of the object c_o and reference c_r can be mismatched, the term of $O_i R_i^*$ will contain a residual parabolic phase with curvature $c' = c_o c_r/(c_r - c_o)$. Any parabolic phase results in a broadening of the ± 1 orders in the Fourier spectrum. Figure 3(a) shows an experimental spectrum of a typical EWI-DWDH hologram and a zoomed-in view of one of the off-axis terms. The broadening of the spectrum is clearly seen in the diagonally distributed off-axis terms. Despite the broadening, the diffraction orders are well separated because of the carefully chosen incidence angle.

From an analysis of the spectrum, many parameters can be estimated.[36–39] For example, the residual wavefront curvature c' is related to the spread of the spectrum Δf_x and Δf_y, which is given by $\Delta f_x = N_x \Delta x/(\lambda_i c')$ along the x direction and $\Delta f_y = N_y \Delta y/(\lambda_i c')$
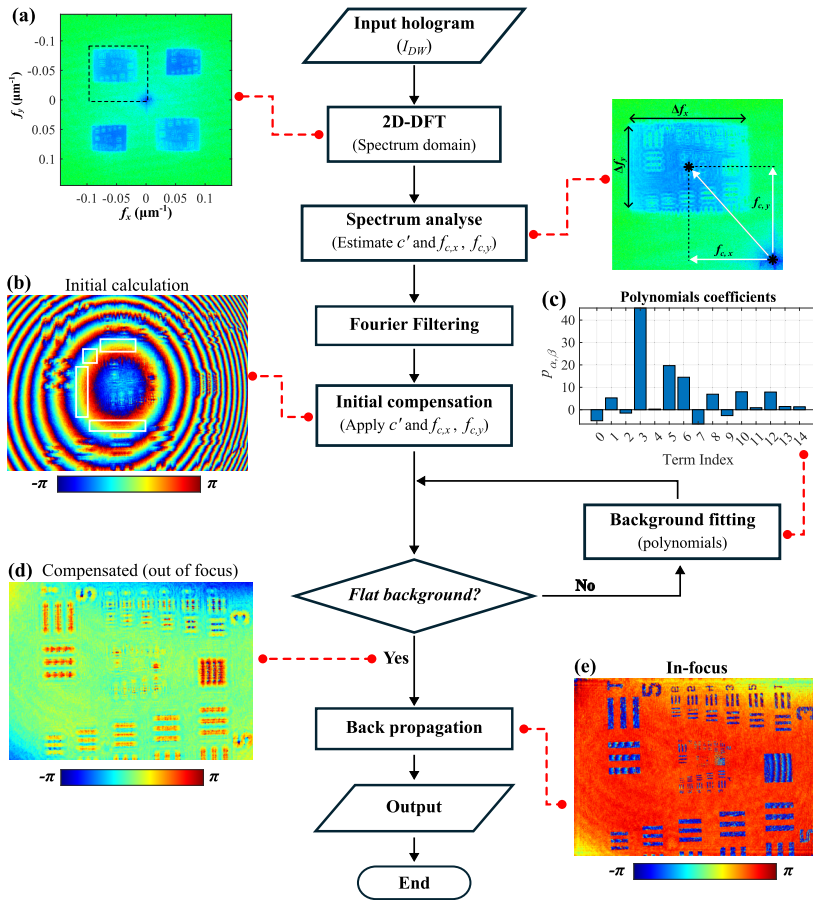
FIG. 3. Data processing flow chart for EWI-DWDH. (a) Spectrum of a dual-wavelength hologram with expanding wavefront illumination. (b) Reconstructed phase of the off-axis term after initial compensation for tilt and parabolic phase. (c) Coefficients of the first 15 polynomials fitted from the background. (d) Compensated phase for (b). (e) In-focus phase after backpropagation.

along the y direction. The carrier spatial frequencies can be estimated by measuring the distance between the coordinate's origin and the centroid of the spectrum in the frequency domain, as indicated in Fig. 3(a). The carrier spatial frequencies are expressed as $f_{c,x}$ for the x direction and $f_{c,y}$ for the y direction. Figure 3(b) shows the experimental results of a reconstructed field of one of the off-axis terms after compensating for the slope and parabolic phase calculated using the analysis described above. Clearly visible is a residual parabolic phase due to the imprecise determination of Δf_x and Δf_y. This imprecision arises from estimation errors that, as observed in the spectrum analysis step, originate from the unsharp edges of the off-axis term.

To address this issue, we implement a background fitting loop. Given a sample that contains known flat areas of the same height, we cut the flat areas out and fit an overall background phase map on them. Assuming that the objects located in the dashed boxes of Fig. 3(b) are flat, coplanar, and the phase aberrations are continuous, they give a unique solution. We fit the phase from these areas with the standard polynomial,

$$\phi_{fit}(x,y) = \sum_{\alpha+\beta=0}^{\alpha+\beta=\gamma} p_{\alpha,\beta} x^{\alpha} y^{\beta}, \tag{7}$$

where γ is the order of the fit and $p_{\alpha,\beta}$ are the weight coefficients. For a specific order, there are $(\gamma+1)(\gamma+2)/2$ coefficients. In our experience, we found that fourth-order ($\gamma = 4$) is sufficient to cope with the phase distortions caused by aberrations that may be encountered.

Figure 3(c) shows the coefficients of the first 15 polynomials of the fitted result. It shows that the major components fall into the third and fifth terms, which correspond to x^2 and y^2 spatial dependence. This result aligns with our expectation; Fig. 3(b) shows that the spherical phase is dominant. Figure 3(d) shows the results after compensating for the fitted phase, which displays a homogeneous phase background, similar to a sample illuminated by a plane wave. Subsequently, the in-focus field [Fig. 3(e)] is obtained through angular spectrum backpropagation of the equivalent distance z_e (see Appendix A for more details). However, note that when using the camera coordinates (x, y) instead of the scaled coordinates $\left(\frac{x}{M_a}, \frac{y}{M_a}\right)$, the actual backpropagation distance becomes $z_e M_a^2$ (or equivalently $z_o M_a$). The magnification M_a can be calibrated using a well-defined sample, such as a resolution target. Subsequently, the setup parameters z_o, z_s, c_r can be determined accordingly. The same data-processing procedures apply to the off-axis term for the second wavelength. If necessary, image registration is performed to correct

for minor misalignment between the two on-focus images. Rigid registration is applied by circular shifting one image relative to the other. The cross-correlation coefficient is used as the similarity metric: the shift that produces the highest coefficient is chosen, and the image is translated accordingly to achieve optimal alignment.

D. Laser calibration and tunability

Increasing the depth range of DWDH requires a large synthetic wavelength, which is equivalent to reducing the separation between the two wavelengths. Therefore, we use a highly stable, non-tunable He–Ne laser with a wavelength of λ_1 = 632.992 nm. As a second wavelength (λ_2) source, we use a tunable external cavity diode laser (ECDL) operating at ~633 nm, which can be slightly tuned in wavelength by adjusting the diode temperature or drive current. The key challenge for obtaining a large synthetic wavelength is to accurately calibrate the operating wavelength of the ECDL. Achieving a cm-scale synthetic wavelength Λ requires λ_2 to be separated less than 40 pm from the wavelength of the He–Ne laser. A high-resolution wavemeter could address this problem by externally monitoring λ_2. However, a high-resolution wavemeter is not always available. Here, we propose a simple and practical method for calibrating the wavelength of ECDL. The proposed method involves using the DWDH setup to measure a sample with a well-defined step height. With the reconstructed beat phase Φ, (4) can be applied to calculate the synthetic wavelength, $\Lambda = 4\pi h/\Phi$. Assuming stable He–Ne laser operation at λ_1, λ_2 can be calculated as

$$\lambda_2 = \frac{4\pi h \lambda_1}{4\pi h - \lambda_1 \Phi}. \tag{8}$$

This calibration was performed with a sample with several grooves with well-defined depths (Rubert & Co Ltd, product type 515). The groove with a depth of 1000 µm was selected for calibration. To ensure complete imaging of the entire sample, the calibration was performed without using expanding wavefront illumination. Figure 4(a) shows the reconstructed complex field for synthetic wavelength from our DWDH setup (ECDL operating at T = 18 °C and I = 91 mA), where the image brightness indicates the reflected intensity and the color represents the synthetic phase. The bottom of the grooves has a distinctly different phase value compared to the surrounding surface; the black areas are locations where, due to shadowing, no reflected light reaches the camera. Figure 4(b) shows the cross section profile along the red dashed line in (a). The phase distribution on both sides of the grooves is not entirely flat due to the slight curvature of the workpiece surface. The plot
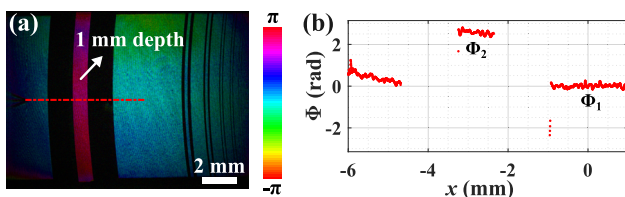
FIG. 5. Drive current tuning of wavelength of the external cavity diode laser (ECDL) at T = 18 °C. The right-hand axis indicates the obtained synthetic wavelength.

exhibits a clear phase contrast with sharp transitions, indicating the distinct height change. To mitigate the effect of phase fluctuations, the phase value is calculated by selecting a small region and averaging the values within it. Thirty repeated experiments yield a result of Φ_{2-1} = 2.48 ± 0.09 rad with respect to the relative phase of the groove. Using the specified groove depth of 993.554 µm, we calculated Λ = 5.04 ± 0.18 mm and λ_2 = 633.072 ± 0.003 nm.

The wavelength of the ECDL can be tuned by adjusting either the drive current or the diode temperature. In general, the wavelength λ_2 decreases with decreasing temperature and drive current. Using the same calibration procedure, we investigated the tunability of the ECDL. Figure 5 presents the calibration results for λ_2 at T = 18 °C with drive currents I ranging from 81 to 95 mA. For each drive current, 30 measurements were performed, where the error bars in the plot represent the statistical standard deviation. The wavelength of the He–Ne laser (λ_1 = 632.992 nm) is plotted as the red dashed line in the plot. The results indicate that the ECDL undergoes mode hopping near drive currents of 82 and 93 mA. Between these points, λ_2 increases with increasing drive current, in agreement with the data provided by the manufacturer. Although additional λ_2 calibrations can be performed at different temperatures or drive currents, this demonstration shows the ability to precisely control both λ_2 and Λ.

III. LATERAL RESOLUTION ENHANCEMENT RESULTS

The experimentally achievable resolution and field of view (FOV) were evaluated using a USAF resolution target. In lensless digital holography with PWI, the lateral resolution is mainly constrained by the NA and the sensor pixel size Δx. Figures 6(a) and 6(b) show the experimental results of optical field reconstruction under this configuration, where the FOV corresponds to the sensor size (10.38 × 14.19 mm² in our case). The sample-to-sensor distance, determined by visual optimization of image sharpness, is z_o = 46.61 mm, resulting in a theoretical resolution limit of r_a = 4.66 µm. However, since this value is smaller than twice the pixel size ($2\Delta x$ = 6.9 µm), the achievable PWI resolution is limited to 6.9 µm. Figure 6(b) provides a zoomed-in view of the white dashed box in Fig. 6(a), showing that the patterns of "group 4 and 5" are distinguishable. The smallest distinguishable pattern is "group 6–1," its cross profile is plotted as the blue line in Fig. 6(e). The nominal line spacing in "group 6–1" is 7.81 µm, which can be considered as the effective resolution of the PWI system and closely approximates the expected resolution limit of two pixels.

Figures 6(c) and 6(d) present the results obtained with EWI. As illustrated in Fig. 2, the lateral resolution in lensless EWI-DWDH can be smaller than two pixels $2\Delta x$ as long as the configuration of the setup satisfies the condition in (6). From the reconstructed

FIG. 4. λ_2 calibration with a standard height sample. (a) Retrieved complex field of the sample, where the brightness indicates the amplitude and the color indicates the phase. (b) Cross section of the phase along the red dash line in (a).
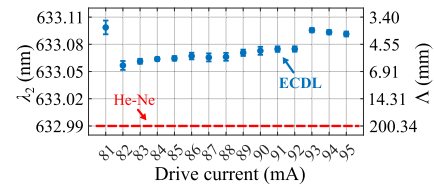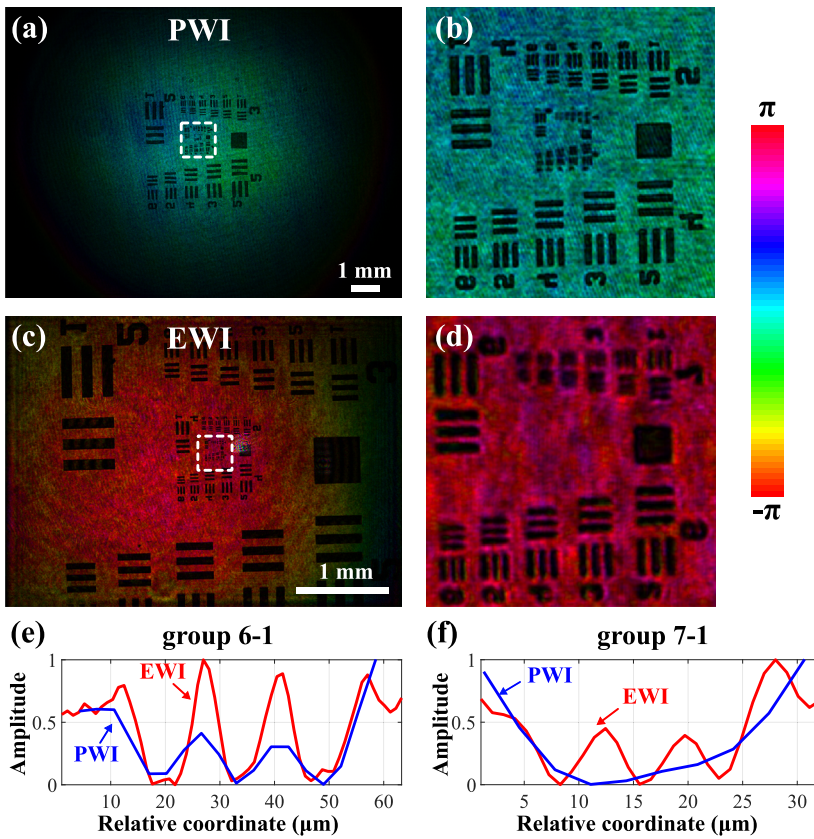
FIG. 6. Achievable lateral resolution comparison in dual-wavelength digital holography. [(a) and (b)] Reconstructed field for plane wavefront illumination (PWI). [(c) and (d)] Reconstructed field for expanding wavefront illumination (EWI). (e) Comparison of cross profile plot of pattern in "group 6–1." (f) Comparison of cross profile plot of pattern in "group 7–1."

image in Fig. 6(c), the magnification is determined as $M_a = 3.35$ by comparing the measured line spacing with the specified value. The sample-to-sensor distance is determined to be $z_o = 41.22$ mm. This closely matches the value measured with a ruler and differs slightly from the PWI presented in the previous paragraph because the two measurements were conducted independently. The distance z_s is calculated as 17.55 mm based on the relationship $M_a = (z_o + z_s)/z_s$. These parameters yield a theoretical diffraction limit of $r_a = 4.16$ µm, achievable as long as $z_s \leq 23.93$ mm. Since this condition for z_s is satisfied, the theoretical diffraction limit is NA limited to $r_a = 4.16$ µm. Figure 6(d) provides a zoomed-in view of the white dashed box in Fig. 6(c), showing that the pattern of "group 7–1" is just distinguishable, as can be seen from its cross section profile that is plotted as the red line in Fig. 6(f). The nominal line spacing in "group 7–1" is 3.91 µm, demonstrating the ability of EWI-DWDH to enhance resolution and break the pixel-size resolution limit. This resolution enhancement comes at the cost of a reduced lateral FOV, which, in EWI-DWDH, is scaled down by a factor of M_a. This reduction is evident when comparing the imaged object sizes in Figs. 6(a) and 6(c).

IV. LARGE HEIGHT MEASUREMENTS RESULTS

To demonstrate our large DWDH depth-range measurement capability, we measured a stepped sample, of which its surface covers a large height range. The sample was made of brass and

machined with a high-precision CNC machine (Fehlmann, PICO-MAX 56L TOP). It has multiple height steps with a height increment of 0.5 mm, as shown in Fig. 7(a). The hologram were recorded in a single-shot acquisition with an exposure time of around 200 µs. The ECDL operated at a temperature of $T = 8.5\,°C$ and a drive current of $I = 87$ mA, with the synthetic wavelength and the ECDL wavelength calibrated as $\Lambda = 9.17 \pm 0.25$ mm and $\lambda_2 = 633.0360 \pm 0.0012$ nm, respectively. Figures 7(b) and 7(c) show the reconstructed complex
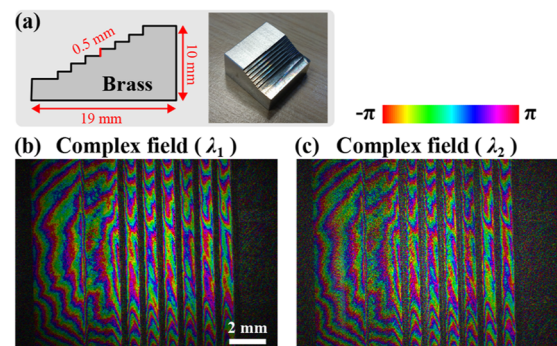

FIG. 7. (a) Schematic on the left is a dimensional drawing of the stepped sample, and the photograph of it is on the right. Each step has a height of 0.5 mm. [(b) and (c)] The retrieved field for the two laser wavelengths.

fields for He–Ne and ECDL separately. In the field maps, brightness indicates the wave intensity and color represents the phase. Both maps share the same color and scale bar. The results clearly show distinct well-separated strips that are the steps of the sample. The phase values indicate depth variations, enabling the extraction of surface topography information. However, the inhomogeneous phase distribution at each step indicates surface irregularities, which appear on a scale larger than half the wavelength. Moreover, every step contains a few wrapped cycles of the phase, indicating fluctuations on the order of 1 μm. Given the precision of the CNC machine (around 5 μm), this level of roughness is reasonable.

The two individual phase maps in Fig. 7 show phase wrapping due to the large step height and height variation. Without additional information, phase unwrapping algorithms cannot resolve such sharp phase jumps. Figure 8(a) presents the result of applying a phase unwrapping algorithm[15] to the results in Fig. 7(b). The steps are all mapped to the same height because the phase jumps are very large, and there are areas where no phase information is available. This shows that the stepped structure cannot be reconstructed from single-wavelength DH. In DWDH, this issue is addressed by calculating the beat phase and the unambiguous height map is computed with (4). The reconstructed height map is presented in Fig. 8(b), where all the steps, visualized with different colors, are distinguishable. Since each step is effectively flat on the millimeter scale, it is displayed in a relatively uniform color corresponding to its height. The inset displays the cross section along the black dashed line, providing a clearer visualization of the reconstruction of the stepped structure. From right to left, each step rises around 0.5 mm higher than the preceding one, as expected. The results demonstrate a successful measurement of all the steps without wrapping because the synthetic wavelength $\Lambda = 9.17 \pm 0.25$ mm covers the entire 3.5 mm height range of the sample. To further demonstrate the single-shot, high-speed DWDH imaging capability, measurements of a moving

object were performed (Multimedia available online). The 3D perspective image in Fig. 8(c) clearly illustrates the stepped stairs and the increase in height. For quantitative comparison, we set the rightmost step as the baseline and determined the relative heights of the remaining steps by averaging the height values from randomly selected small regions within each step, avoiding step boundaries to prevent averaging errors. The same procedure was applied to both our measurement and the white-light interferometer data (WLI, Bruker ContourGT-K). Figure 8(d) shows results with the horizontal axis showing the reference height measured by WLI, and the orange points represent the mean heights measured by our DWDH setup at $\Lambda = 9.17$ mm with error bars indicating standard deviation within each region. Spatial averaging in a center region minimizes edge effects and reduces noise. The black dashed line, with a slope of unity, serves as a reference.

To assess the versatility of our method, we also performed measurements on objects with height variations exceeding 1 cm. The results, which are presented in Appendix B, confirm that the setup can quantitatively measure heights for cm-scale and potentially larger depth ranges. Since the height difference in this case surpasses the measurement range of our WLI system, no WLI reference data are provided.

V. INSTANTANEOUS AND TEMPORAL PRECISION

The DWDH phase measurements are affected by multiple noise sources, including speckle decorrelation noise, shot noise, and environmental disturbances, such as mechanical vibrations and air currents.[40–42] Although noise is inherent in practical measurements, analyzing its sources and impact provides crucial insights into measurement precision. The single-shot measurement nature of our proposed method, with acquisition times under a ms, minimizes the impact of ambient disturbances on individual measurements. However, the effect of these disturbances on long-time stability needs further investigation, as we will do here.

Instantaneous precision characterizes the reliability of a single DWDH measurement and is mainly influenced by speckle decorrelation and noise. Speckle decorrelation noise is caused by surface roughness. When the laser light scatters off a rough surface, microscale irregularities induce random phase shifts to the scattered wavefronts. The resultant constructive and destructive interferences generate grainy speckle intensity patterns with a partially random phase. Increased levels of surface roughness enhance these phase variations, causing the speckle patterns to decorrelate more rapidly, resulting in more pronounced phase fluctuations. Technical noise sources include shot noise, quantization noise, dark noise, and laser intensity fluctuations or relative intensity noise. Among these, shot noise is the fundamental limitation in phase-reconstruction precision. According to the model developed by Gong and Piniard,[40,43] the phase retrieval precision from an off-axis hologram is

FIG. 8. Height map reconstruction of the stepped sample. (a) Result of applying the phase unwrapping algorithm. (b) Results of single-shot dual-wavelength digital holography at $\Lambda = 9.17$ mm. High speed DWDH imaging is demonstrated with a dynamic measurement (Multimedia available online). (c) 3D perspective view of the result of (b). (d) Relative steps height for dual-wavelength digital holography and white light interferometry.

$$\sigma_\phi = \sqrt{\frac{4 \cdot \text{FR}}{V^2 \alpha^2}\left[\frac{\alpha}{N_{sat}} + \frac{1}{12(2^{nbit} - 1)^2}\right] + \left(\frac{7}{4}\right)^2 \left(\frac{8\pi^2 R_a^2}{\Lambda^2}\right)^{\frac{4}{5}}}, \quad (9)$$

where FR is the filter ratio of the filter window size used to extract the off-axis terms to the total spatial bandwidth of the sensor in the spatial frequency domain, N_{sat} is the full well capacity of a pixel, and *nbit*
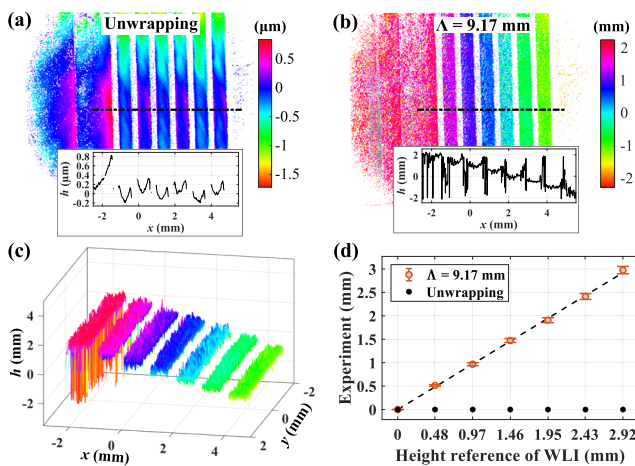
indicates the image bit depth. The parameters V and α represent the modulation depth (or fringe visibility) and saturation of the hologram, respectively. R_a is the surface roughness. Under the square root, the first term corresponds to the shot noise contribution, the second term represents the quantization noise contribution, and the third term accounts for the speckle decorrelation noise. Dark noise and readout noise are excluded from consideration in (9) as we will show them to be negligible.

To isolate the system from speckle decorrelation noise effects, a mirror was used as a test sample. The theoretical phase precision was calculated using (9) for a hologram captured with a camera having $N_{sat} = 9900e^-$ and recorded as a grayscale image of $nbit = 8$. The exposure time was around 200 μs and was maximized without causing overexposure. Additional parameters were determined during data processing. For example, the modulation depth of the hologram V was calculated as $V_i = 2AC_i/DC$, where AC_i is the amplitude of the off-axis term and DC is the amplitude of the constant background bias. Both values are obtained through Fourier filtering and are spatially dependent. In DWDH, the DC bias is a superposition of the individual DC biases from two lasers and cannot be separated without additional measurements. Similarly, since the individual hologram saturation α cannot be determined independently, we assume they are equivalent for both lasers, leading to $\alpha = 0.5 \cdot DC/(2^{nbit} - 1)$. The resulting theoretical precision values σ_ϕ^T are 18.0 mrad for the He–Ne laser and 12.9 mrad for the ECDL. The theoretical beat phase precision σ_Φ^T is calculated as 22.1 mrad by computing the square root of their summed squares.

Experimental evaluation of the instantaneous phase precision was performed through differential measurements: the phase map of one hologram was subtracted from that of the subsequent hologram. This process cancels out constant illumination aberrations that would otherwise bias the calculated spatial phase variance. The analysis focused on a central 256×256 pixel region with relatively uniform amplitude. Figure 9 shows the beat phase map (a) and its statistical distribution (b). Ideally, the phase across the mirror should be constant; however, the observed fluctuations—displayed as a quasi-Gaussian distribution in the histogram [Fig. 9(b)]—indicate the presence of noise. The experimental measurement yielded a standard deviation of $\sigma_\Phi^E = 31.1$ mrad, which is slightly higher than the theoretical expected precision σ_Φ^T. This discrepancy may be attributed to data imperfections, including parasitic fringes caused by coherent laser diffraction and internal optical reflections superimposed on the hologram. The Gaussian shape of the phase distribution is in agreement with the predominance of shot-noise,
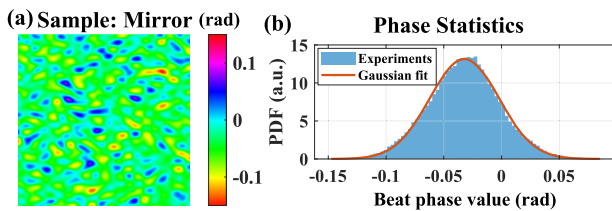
since the high surface flatness (peak-to-valley: 63 nm) leads to low decorrelation noise (0.75 mrad phase deviation).

The temporal precision of the phase measurements was investigated using 10 000 consecutive holograms from a mirror, acquired at a rate of 100 Hz. A specific point was selected from the retrieved phase maps, and its phase value was tracked over time. Figure 10(a) displays the time series of the phase at this point showing from top to bottom the He–Ne laser field phase ($\phi_{\text{He-Ne}}$), the ECDL field phase (ϕ_{ECDL}), and the beat phase (Φ). All three signals exhibited significant temporal phase fluctuations, an expected outcome considering the ambient vibrations in the laboratoy and the inherent sensitivity of phase measurement. Power spectral density (PSD) analysis [Fig. 10(b)] reveals local maxima at 38 and 47 Hz in both $\phi_{\text{He-Ne}}$ and ϕ_{ECDL}. These spectral peaks are absent in the PSD plot of Φ, suggesting that a common noise source—possibly camera noise or sample jitter—affects the phase of both lasers equally and cancels out during the beat-phase calculation.

However, the time-domain plot of the absolute beat phase Φ still exhibits significant fluctuations. The corresponding PSD shows that while the data are free from characteristic frequency noise, perturbations at 9 Hz and its integer multiples are visible, although their origin remains unidentified. The strong temporal jitter in the absolute beat phase Φ can be attributed to the non-common path system, in which the two arms are exposed to different environmental disturbances. In this case, the effect of vibrations manifests itself in frame-to-frame uncertainty and can be treated as random noise over long time periods. We mitigated this issue by selecting two points on the sample and calculating the relative phase difference, $\Delta\Phi$. The result, shown in Fig. 11(a), demonstrates that the phase variation is significantly reduced. The PSD plot of $\Delta\Phi$ has a pattern similar to that of the absolute phase Φ but with a significantly reduced amplitude. This provides indirect confirmation of the temporal randomness of the noise, as its elimination results in an overall background reduction in the PSD plot.

To further elucidate the cause of the noise, we applied an Allan variance analysis,[44] which is a widely used and effective tool for characterizing temporal stability, providing insights into various noise types and long-term drift behavior. In the Allan variance analysis, the time series phase data are segmented into sections of equal duration τ and the phase is averaged. Then, it quantifies how much the time average of each section differs from that of the previous average, mathematically expressed as

$$\sigma_{\Delta\Phi}^2(\tau) = \frac{1}{2}\langle(\overline{\Delta\Phi}_{i+1} - \overline{\Delta\Phi}_i)^2\rangle, \quad (10)$$

where $\langle . \rangle$ denotes temporal averaging and $\overline{\Delta\Phi}_i$ is the ith sample of the average of $\Delta\Phi$ over observation time τ. Figure 11(b) shows an Allan deviation ($\sqrt{\sigma^2(\tau)}$) analysis of $\Delta\Phi$ and is plotted on a log–log scale, with τ ranging from 0.02 s to around 33 s. The calculated Allan deviation from the experimental data are represented by the blue curve, accompanied by two trend lines illustrating different noise components: shot noise (shown in red), which has a slope of $\tau^{-0.5}$, and systematic drift (shown in yellow), which has a slope of τ^1. For short averaging times ($\tau < 1$ s), the Allan deviation $\sigma(\tau)$ decreases with a slope similar to the shot noise line. As the averaging time increases, systematic drift becomes dominant, causing $\sigma(\tau)$ to increase roughly
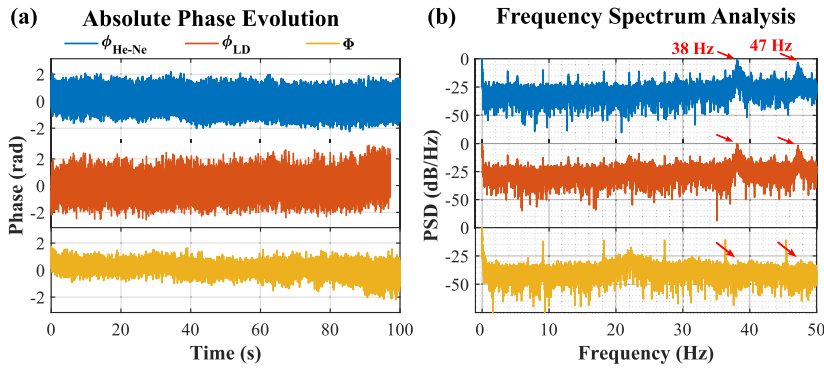

FIG. 9. (a) Single frame beat phase map Φ on a central area of a mirror. (b) Statistical distribution of the beat phase values in (a).

FIG. 10. (a) Time resolved results of three phase values at one point: He–Ne laser field phase (ϕ_{He-Ne}), ECDL field phase (ϕ_{ECDL}), and beat phase (Φ). (b) Corresponding power spectral density (PSD) analysis.
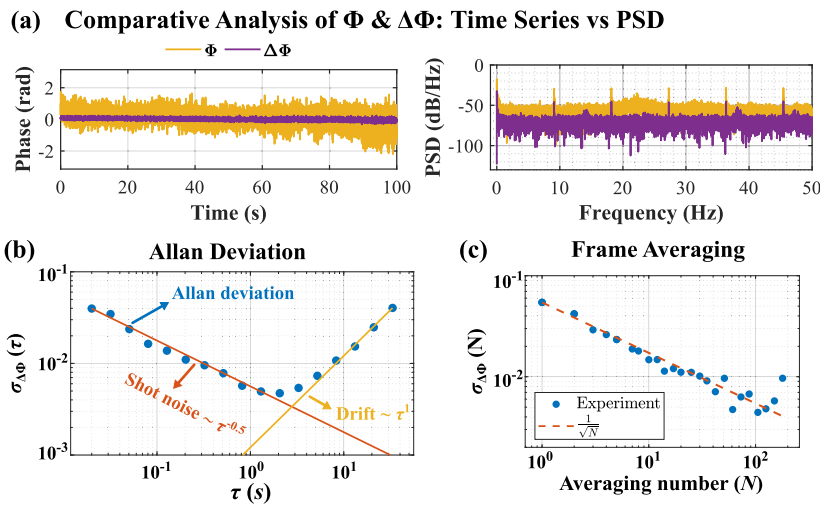

FIG. 11. (a) Comparative analysis of Φ and $\Delta\Phi$ in the time and frequency domain. (b) Allan deviation analysis regarding $\Delta\Phi$. (c) Standard deviation of the synthetic phase vs frame number showing the reduction of the noise upon averaging.

as τ^1. The minimum occurs around $\tau = 1$–2 s, indicating the maximum averaging duration to achieve minimal signal noise before drift becomes dominant. The predominance of shot noise on short time scales was verified by comparing the measured standard deviation σ against the frame averaging number (N), as shown in Fig. 11(c). The experimental data points (blue dots) closely align with the theoretical prediction of $1/\sqrt{N}$ (dashed red line), confirming the shot noise as the primary noise source at short time scales.[41,42]

VI. DISCUSSION

The height measurement precision of DWDH is fundamentally determined by the phase measurement accuracy, which in our setup is primarily limited by shot noise. We achieve an experimental phase measurement accuracy of $\sigma_\Phi^E = 31.1$ mrad. As described by (4), the height error scales linearly with the synthetic wavelength Λ, which, for our setup, results in $\sigma_h = \sigma_\Phi^E/(4\pi) \cdot \Lambda = 0.24\%\Lambda$. Phase averaging techniques can effectively improve phase precision by a factor of $\sqrt{N}$ in shot-noise-limited detection, where N is the number of averaged frames, as shown in Fig. 11. Practical implementation in our setup allows for averaging up to 100 frames [see Fig. 11(c)], thereby providing up to tenfold improvement. In addition, frame averaging

compromises the single-shot nature of our approach and may introduce errors due to lateral sample drift.

To preserve the advantages of single-shot measurement, an approach to obtain better height sensitivity is to use more optical power to reduce relative phase noise. In principle, the single-shot height measurement range is infinite. We have shown height measurements in excess of 1 cm, see Appendix B. However, further extending this range will be limited by the wavelength stability of both lasers and the accuracy of the calibration method. Another approach to obtain an improved height sensitivity is to use the tunability of Λ to optimize the height precision for a given sample, where the highest precision is obtained by choosing Λ just larger than twice the expected height difference. In addition, although median filtering was applied to suppress high-frequency noise in our results, further improvement is possible. Advanced denoising techniques, both numerical and experimental strategies, could be explored in the future work to further enhance measurement precision.

Although DWDH can be performed using a single light source combined with acousto-optic modulators (AOMs),[22] the selection of the ECDL as secondary light source was motivated primarily by three considerations.

First, the ECDL provides relatively broad wavelength tunability. Similarly to Fig. 5, which shows the operating wavelength of the ECDL at $T = 18\,^\circ$C, we performed wavelength calibrations at various temperatures (T) and drive currents (I). These results show wavelength overlap with the emission band of the He–Ne laser and a tuning range up to a maximum wavelength of 633.756 nm (achieved at $T = 30\,^\circ$C and $I = 103$ mA). Based on this tuning range, the synthetic wavelength Λ can be varied from 0.53 mm to effectively infinity. In contrast, AOM-based approaches generally only provide a frequency shift less than 1 GHz, which restricts the synthetic wavelength to $\Lambda \geq 300$ mm.

Second, the ECDL provides application-specific height resolution control. Considering that the height precision is linear to Λ and that semiconductor products have height variations in the sub-mm to cm-scale range, the use of an ECDL provides better height resolution and sensitivity. However, the ECDL mode hopping may occur during ECDL tuning, and operating at the extremities of the tuning range can induce output instability, resulting in linewidth broadening and coherence degradation. These effects should be carefully avoided, for example, by using an ECDL frequency locked to the He–Ne laser.[45]

Third, ECDL power generation is efficient. Although commercial low-frequency AOMs can achieve 70%–90% first-order diffraction efficiency, their performance is highly sensitive to angular alignment and thermal stability. In contrast, high-frequency AOMs suffer from significant losses, as exemplified by a mere 11% diffraction efficiency for a 5 GHz frequency shift.[46] This technical limitation becomes critical when considering the generation of cm-scale synthetic wavelengths, where the required frequency shift exceeds 30 GHz. In addition, because the dual-wavelength scheme requires use of the zero- and first-order transmitted beam as well, this imposes high demands on the laser power.

This paper demonstrates that expanding wavefront illumination breaks the pixel size limitation on spatial resolution, leaving it only constrained by the NA of the system. Hence, the demonstrated spatial resolution of 3.91 μm, as shown in Fig. 6, is not the fundamental limit. Reduction of the sample–sensor distance can improve resolution, but practical constraints arise from the physical dimensions of the beam splitter that limit the reduction of the object to sensor distance. An alternative approach involves using larger-size detectors, where the demonstrated decoupling of resolution from the pixel size allows the use of larger-pixel sensors while maintaining the resolution enhancement potential.

VII. CONCLUSION

In this paper, we demonstrated a lensless, single-shot dual-wavelength digital holography scheme with expanding wavefront illumination (EWI-DWDH). Our method overcomes the pixel-size limitations inherent in the spatial resolution of conventional digital holography systems. Experimental results demonstrate that the EWI-DWDH enhances spatial resolution to 3.91 μm (smaller than two pixels 6.9 μm) and is in agreement with the diffraction-limited theoretical predictions. Moreover, by combining a tunable diode laser with a He–Ne laser, a centimeter-scale depth measurement range is achieved, thereby broadening the applicability of digital holography in 3D industrial inspection. With respect to measurement precision, the single-shot nature of our approach yields results

that approach shot-noise limited detection efficiency. However, systematic drift does affect the measurements for long-time operation. In summary, the proposed scheme provides an efficient and precise 3D inspection tool for industrial fields with stringent requirements for high speed, high resolution, wide field-of-view, and high precision, such as semiconductor manufacturing.

AUTHOR DECLARATIONS

Conflict of Interest

The authors have no conflicts to disclose.

Author Contributions

Huangcheng Shangguan: Conceptualization (equal); Data curation (equal); Formal analysis (equal); Methodology (equal); Validation (equal); Visualization (equal); Writing – original draft (equal); Writing – review & editing (equal). **H. Paul Urbach**: Project administration (equal); Supervision (equal); Writing – review & editing (equal). **Jeroen Kalkman**: Conceptualization (equal); Funding acquisition (equal); Project administration (equal); Supervision (equal); Writing – review & editing (equal).

DATA AVAILABILITY

The data underlying the results presented in this paper and the relevant analysis routines are available at Zenodo: https://doi.org/10.5281/zenodo.16738969.

APPENDIX A: THE EQUIVALENT PROPAGATION DISTANCE

Considering the model illustrated in Fig. 1(b), and assuming that the sample field is $U(\xi, \eta)$, the optical field of the sample illuminated with a spherical wave right after the sample could be written as

$$U_1(\xi, \eta) = U(\xi, \eta) \exp\left[\frac{i\pi}{\lambda z_s}(\xi^2 + \eta^2)\right]. \tag{A1}$$

This field propagates a distance z_o to the camera plane, assuming the paraxial approximation holds in this propagation (i.e., $z_o \gg \sqrt[3]{\pi D^4/(4\lambda)}$, where D is the diameter of the sample), then the object field at the camera plane can be described by the Fresnel diffraction integral,[37]

$$U_2(x, y, z_o) = \exp\left[\frac{i\pi}{\lambda z_o}(x^2 + y^2)\right] \iint U_1(\xi, \eta)$$
$$\times \exp\left[\frac{i\pi}{\lambda z_o}(\xi^2 + \eta^2)\right] \exp\left[-\frac{i2\pi}{\lambda z_o}(x\xi + y\eta)\right] d\xi d\eta. \tag{A2}$$
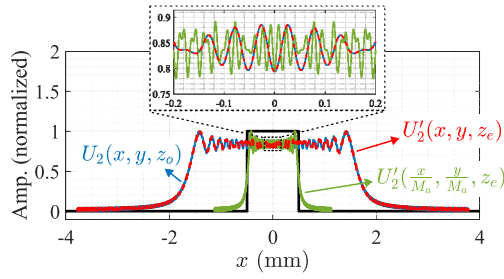
FIG. 12. Comparison of diffraction amplitudes calculated with two different methods.

Notably, substituting (A1) into the integral and defining $z_e = z_o z_s / (z_o + z_s)$ and $M_a = (z_o + z_s)/z_s$, the first two parabolic terms in the integrand can be combined and the last exponential term can also be rewritten, producing the integrand having an expression as

$$U(\xi, \eta) \exp\left[\frac{i\pi}{\lambda z_e}(\xi^2 + \eta^2)\right] \exp\left[-\frac{i2\pi}{\lambda z_e}\left(\frac{x}{M_a}\xi + \frac{y}{M_a}\eta\right)\right]. \quad (A3)$$

The variable z_e is what we call the equivalent propagation distance and M_a is the magnification factor. The physical meaning of these parameters will become clearer in the following derivation. A closer examination of (A3) reveals that it also takes the form of a Fresnel diffraction integral, except that it lacks a parabolic phase term for the scaled coordinates $\left(\frac{x}{M_a}, \frac{y}{M_a}\right)$, and the propagation distance is replaced by z_e. Therefore, (A2) can be expressed as

$$U_2(x, y, z_o) = \exp\left[\frac{i\pi}{\lambda(z_o + z_s)}(x^2 + y^2)\right] \cdot U_2'\left(\frac{x}{M_a}, \frac{y}{M_a}, z_e\right), \quad (A4)$$

$$U_2'\left(\frac{x}{M_a}, \frac{y}{M_a}, z_e\right) = \iint U(\xi, \eta) \exp\left\{\frac{i\pi}{\lambda z_e}\left[\left(\frac{x}{M_a} - \xi\right)^2 + \left(\frac{y}{M_a} - \eta\right)^2\right]\right\} d\xi d\eta. \quad (A5)$$

Equations (A4) and (A5) imply that the field $U_2'\left(\frac{x}{M_a}, \frac{y}{M_a}, z_e\right)$ is essentially a geometrically magnified sample field $U(\xi, \eta)$ illuminated by a plane wave and propagating an equivalent distance z_e. The object field $U_2(x, y, z_o)$ is essentially $U_2'\left(\frac{x}{M_a}, \frac{y}{M_a}, z_e\right)$ with a superimposed parabolic phase distribution. To validate this equivalence, we conducted numerical simulations using a rectangular function as input. Figure 12 shows a simulated comparison of diffraction amplitudes. The black line is the input, and the blue curve represents the theoretical prediction from (A2) with a propagation distance $z_o = 41.22$ mm (the same value as Sec. III). The green curve shows the object field with plane wave illumination and propagating the equivalent distance $z_e = 12.31$ mm, as given by (A5). After applying coordinate scaling to the green curve, the result (red dashed line) shows perfect agreement with the prediction (blue). The inset in the figure shows more clearly the role of coordinate scaling and the equivalence of two methods.

APPENDIX B: VALIDATION OF CENTIMETER-SCALE DEPTH MEASUREMENT

To validate the capability of the method for centimeter-scale depth measurements, we measured a combined object consisting of a 10-mm step and a standard height sample. This arrangement enabled simultaneous wavelength calibration and height measurement in a single acquisition. Figure 13(a) shows the object. The beat phase map reconstructed by our system is presented in Fig. 13(b). The wavelength calibration procedure follows that
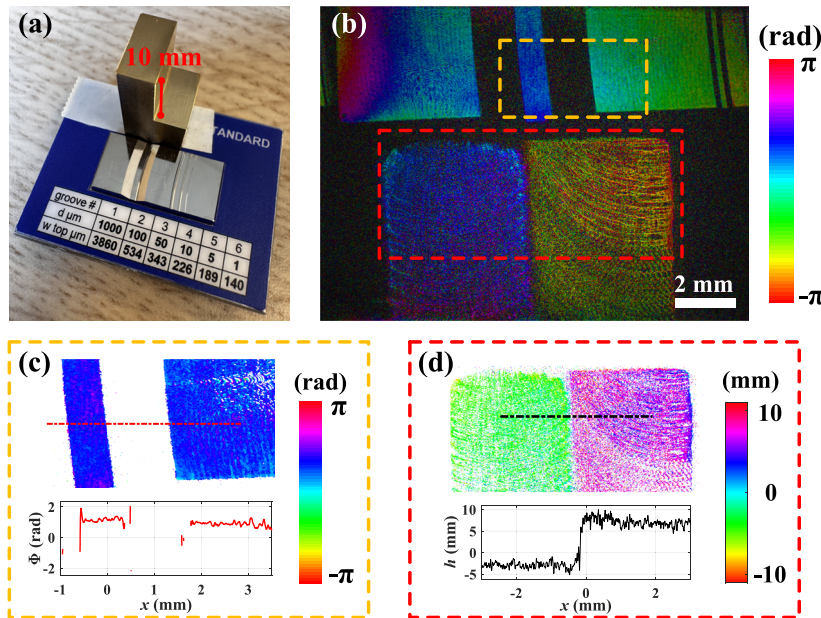

FIG. 13. (a) Object with a 10 mm step and standard height sample. (b) Reconstructed beat phase map. (c) Reconstruction on the standard-height sample [yellow box in (b)] for the wavelength calibration. (d) Height map and cross profile for the step measurement.

described in the main text. After compensating for tilt in the yellow box region, Fig. 13(c) displays the phase map and the cross-sectional profile for standard height measurement. From the known groove depth and phase difference, the synthetic wavelength and the ECDL wavelength were determined as $\Lambda = 44.52 \pm 8.15$ mm and $\lambda_2 = 633.0010 \pm 0.0013$ nm (from 20 measurements and the ECDL operated at $T = 9.4\,°C$ and $I = 96$ mA).

After calibration, the height of the step in the red box region can be quantified using the obtained synthetic wavelength. Figure 13(d) shows the processed phase map (tilt-compensated and converted to height), along with the cross-sectional profile. The step height was measured as 10.31 ± 0.256 mm. Due to the rough surface, some fluctuations are observed, so the reported value is the average over small regions. These results confirm the effectiveness of our method for achieving centimeter-scale depth measurements and potential larger synthetic wavelengths.

REFERENCES

[1] R. B. Bergmann, M. Kalms, and C. Falldorf, "Optical in-process measurement: Concepts for precise, fast and robust optical metrology for complex measurement situations," Appl. Sci. **11**, 10533 (2021).

[2] Y. Shimizu, L.-C. Chen, D. W. Kim, X. Chen, X. Li, and H. Matsukuma, "An insight into optical metrology in manufacturing," Meas. Sci. Technol. **32**, 042003 (2021).

[3] Optical Measurement of Surface Topography, edited by R. Leach (Springer, Berlin, Heidelberg, 2011).

[4] S. Catalucci, A. Thompson, S. Piano, D. T. Branson, and R. Leach, "Optical metrology for digital manufacturing: A review," Int. J. Adv. Des. Manuf. Technol. **120**, 4271–4290 (2022).

[5] A. Ivanina, M. Marshall, K. Abrashitova, T. van Leeuwen, and L. V. Amitonova, "Quantitative phase imaging with a multimode fiber," APL Photonics **10**, 046116 (2025).

[6] J. Xu and S. Zhang, "Status, challenges, and future perspectives of fringe projection profilometry," Opt. Lasers Eng. **135**, 106193 (2020).

[7] M.-Y. Fu, Z.-H. Yin, X.-Y. Yao, J. Xu, Y. Liu, Y. Dong, and Y.-C. Shen, "The progress of optical coherence tomography in industry applications," Adv. Devices Instrum. **5**, 0053 (2024).

[8] D. Gabor, "A new microscopic principle," Nature **161**, 777–778 (1948).

[9] E. N. Leith and J. Upatnieks, "Reconstructed wavefronts and communication theory," J. Opt. Soc. Am. **52**, 1123–1130 (1962).

[10] B. Tayebi, M. R. Jafarfard, F. Sharif, Y. S. Bae, S. H. H. Shokuh, and D. Y. Kim, "Reduced-phase dual-illumination interferometer for measuring large stepped objects," Opt. Lett. **39**, 5740–5743 (2014).

[11] E. Cuche, F. Bevilacqua, and C. Depeursinge, "Digital holography for quantitative phase-contrast imaging," Opt. Lett. **24**, 291–293 (1999).

[12] Z. Huang and L. Cao, "Quantitative phase imaging based on holography: Trends and new perspectives," Light: Sci. Appl. **13**, 145 (2024).

[13] J. Huang, S. Zhu, Y. Li, C. Wang, and E. Y. Lam, "Computational polarized holography for automatic monitoring of microplastics in scattering aquatic environments," APL Photonics **10**, 036114 (2025).

[14] H. S. Abdul-Rahman, M. A. Gdeisat, D. R. Burton, M. J. Lalor, F. Lilley, and C. J. Moore, "Fast and robust three-dimensional best path phase unwrapping algorithm," Appl. Opt. **46**, 6623–6635 (2007).

[15] M. A. Herráez, D. R. Burton, M. J. Lalor, and M. A. Gdeisat, "Fast two-dimensional phase-unwrapping algorithm based on sorting by reliability following a noncontinuous path," Appl. Opt. **41**, 7437–7444 (2002).

[16] S. Park, Y. Kim, and I. Moon, "Automated phase unwrapping in digital holography with deep learning," Biomed. Opt. Express **12**, 7064–7081 (2021).

[17] J. Gass, A. Dakoff, and M. K. Kim, "Phase imaging without 2π ambiguity by multiwavelength digital holography," Opt. Lett. **28**, 1141–1143 (2003).

[18] H. Zhou, M. M. R. Hussain, and P. P. Banerjee, "A review of the dual-wavelength technique for phase imaging and 3D topography," Light: Adv. Manuf. **3**, 314–334 (2022).

[19] M. K. Kim, "Phase microscopy and surface profilometry by digital holography," Light: Adv. Manuf. **3**, 481–492 (2022).

[20] M. Piniard, B. Sorrente, G. Hug, and P. Picart, "Melt pool monitoring in laser beam melting with two-wavelength holographic imaging," Light: Adv. Manuf. **3**, 14–25 (2022).

[21] D. Khodadad, E. Hällstig, and M. Sjödahl, "Shape reconstruction using dual wavelength digital holography and speckle movements," Proc. SPIE **8788**, 106–116 (2013).

[22] U. Abeywickrema, D. Beamer, P. Banerjee, and T.-C. Poon, "Holographic topography using acousto-optically generated large synthetic wavelengths," Proc. SPIE **9771**, 69–75 (2016).

[23] A. Wada, M. Kato, and Y. Ishii, "Large step-height measurements using multiple-wavelength holographic interferometry with tunable laser diodes," J. Opt. Soc. Am. A **25**, 3013–3020 (2008).

[24] H. Shangguan, H. P. Urbach, and J. Kalkman, "Lensless single-shot dual-wavelength digital holography for industrial metrology," Appl. Opt. **63**, 4427–4434 (2024).

[25] E. Serabyn, K. Liewer, C. Lindensmith, K. Wallace, and J. Nadeau, "Compact, lensless digital holographic microscope for remote microbiology," Opt. Express **24**, 28540–28548 (2016).

[26] X. Wu, J. Sun, Y. Chen, J. Wei, Q. Chen, T.-C. Poon, P. Gao, and C. Zuo, "Wavelength-scanning pixel-super-resolved lens-free on-chip quantitative phase microscopy with a color image sensor," APL Photonics **9**, 016111 (2024).

[27] Y. Gao and L. Cao, "Iterative projection meets sparsity regularization: Towards practical single-shot quantitative phase imaging with in-line holography," Light: Adv. Manuf. **4**, 37–53 (2023).

[28] Z. Huang and L. Cao, "K-space holographic multiplexing for synthetic aperture diffraction tomography," APL Photonics **9**, 056101 (2024).

[29] E. Serabyn, K. Liewer, and J. K. Wallace, "Resolution optimization of an off-axis lensless digital holographic microscope," Appl. Opt. **57**, A172–A180 (2018).

[30] F. Wicki and T. Latychevskaia, "Double-slit holography—A single-shot lensless imaging technique," Sci. Rep. **14**, 12528 (2024).

[31] S. Na, S. Shin, and Y. Yu, "Digital holographic microscopy using a spherical reference wave and polarization hologram," J. Korean Phys. Soc. **77**, 908–911 (2020).

[32] S. Rehman, K. Matsuda, M. Yamauchi, M. Muramatsu, G. Barbastathis, and C. Sheppard, "A simple lensless digital holographic microscope," in Biomedical Optics and 3-D Imaging (Optica Publishing Group, 2012), p. DSu3C.3.

[33] J. Kühn, T. Colomb, F. Montfort, F. Charrière, Y. Emery, E. Cuche, P. Marquet, and C. Depeursinge, "Real-time dual-wavelength digital holographic microscopy with a single hologram acquisition," Opt. Express **15**, 7231–7242 (2007).

[34] D. G. Abdelsalam, R. Magnusson, and D. Kim, "Single-shot, dual-wavelength digital holography based on polarizing separation," Appl. Opt. **50**, 3360–3368 (2011).

[35] T. Latychevskaia, "Lateral and axial resolution criteria in incoherent and coherent optics and holography, near- and far-field regimes," Appl. Opt. **58**, 3597–3603 (2019).

[36] J. Min, B. Yfao, S. Ketelhut, C. Engwer, B. Greve, and B. Kemper, "Simple and fast spectral domain algorithm for quantitative phase imaging of living cells with digital holographic microscopy," Opt. Lett. **42**, 227–230 (2017).

[37] J. Goodman, Introduction to Fourier Optics, McGraw-Hill Physical and Quantum Electronics Series (W.H. Freeman, 2005).

[38] D. Khodadad, "Phase-derivative-based estimation of a digital reference wave from a single off-axis digital hologram," Appl. Opt. **55**, 1663–1669 (2016).

[39] R. Riesenberg and M. Kanka, "Self-calibrating lensless inline-holographic microscopy by a sample holder with reference structures," Opt. Lett. **39**, 5236–5239 (2014).

[40] L. Gong, G. Penelet, and P. Picart, "Noise and bias in off-axis digital holography for measurements in acoustic waveguides," Appl. Opt. **60**, A93–A103 (2021).

[41] P. Hosseini, R. Zhou, Y.-H. Kim, C. Peres, A. Diaspro, C. Kuang, Z. Yaqoob, and P. T. C. So, "Pushing phase and amplitude sensitivity limits in interferometric microscopy," Opt. Lett. **41**, 1656–1659 (2016).

[42] F. Charriére, B. Rappaz, J. Kühn, T. Colomb, P. Marquet, and C. Depeursinge, "Influence of shot noise on phase measurement accuracy in digital holographic microscopy," Opt. Express **15**, 8818–8831 (2007).

[43] M. Piniard, B. Sorrente, G. Hug, and P. Picart, "Modelling of the photometric balance for two-wavelength spatially multiplexed digital holography," Proc. SPIE **11783**, 1178308 (2021).

[44] D. W. Allan, "Statistics of atomic frequency standards," Proc. IEEE **54**, 221–230 (1966).

[45] J. Biesheuvel, D. W. E. Noom, E. J. Salumbides, K. T. Sheridan, W. Ubachs, and J. C. J. Koelemeij, "Widely tunable laser frequency offset lock with 30 GHz range and 5 THz offset," Opt. Express **21**, 14008–14016 (2013).

[46] C. Zhou, C. He, S.-T. Yan, Y.-H. Ji, L. Zhou, J. Wang, and M.-S. Zhan, "Laser frequency shift up to 5 GHz with a high-efficiency 12-pass 350-MHz acousto-optic modulator," Rev. Sci. Instrum. **91**, 033201 (2020).

22 December 2025 13:36:07